2023-24-0110 Published 28 Aug 2023

Wall Permeability Estimation in Automotive Particulate Filters

Callum Samuels, Ran Holtzman, and Stephen Benjamin Coventry University

Svetlana Aleksandrova University of Leicester

Timothy C. Watling Johnson Matthey

Humberto Medina University of Nottingham

Citation: Samuels, C., Holtzman, R., Benjamin, S., Aleksandrova, S. et al., "Wall Permeability Estimation in Automotive Particulate Filters," SAE Technical Paper 2023-24-0110, 2023, doi:10.4271/2023-24-0110.

Received: 22 May 2023 Revised: 30 Jun 2023 Accepted: 30 Jun 2023

Abstract

Porous wall permeability is one of the most critical factors for the estimation of backpressure, a key performance indicator in automotive particulate filters. Current experimental and analytical filter models could be calibrated to predict the permeability of a specific filter. However, they fail to provide a reliable estimation for the dependence of the permeability on key parameters such as wall porosity and pore size.

This study presents a novel methodology for experimentally determining the permeability of filter walls. The results from four substrates with different porosities and pore sizes are compared with several popular permeability estimation methods (experimental and analytical), and their validity for this application is assessed. It is shown that none of the assessed methods predict all permeability trends for all substrates, for cold or hot flow, indicating that other wall properties besides porosity and pore size are important.

The hot flow test results show an increase in permeability with temperature, which is attributed to the effects associated with slip-flow. It is shown that the slip-effect magnitude also varies with the filter wall properties. Existing models that account for the effect of slip are assessed and are shown to underpredict the effect considerably for all four substrates. This is important for the prediction of through-wall losses in applications where permeability increase with temperature is a desirable effect. Further investigation is needed to consider the effect of the high temperatures in exhaust applications.

Introduction

The arrival of the Euro 7 emissions standard [1] is leading automotive manufacturers to match increasingly stringent emissions targets with increasingly efficient and complex emission control systems. While engine design can play a big role (for example exhaust gas recirculation, direct fuel injection, etc.), the exhaust gas after-treatment devices also play a crucial role [2,3].

After-treatment devices, such as particulate filters, for gasoline or diesel engines (GPF/DPF), can achieve high-efficiency levels of particulate filtration, however, they also create additional backpressure in the exhaust system that can negatively impact engine performance [4, 5, 6, 7]. For this reason, efficient and accurate backpressure and filtration prediction models are required to estimate the backpressure and to manage the trade-off between unwanted pressure losses and filtration efficiency.

One of the most prevalent contributions to the backpressure in particulate filters is the permeation of exhaust gases through the porous filter walls [6, 8, 9, 10]. As the gas travels through the irregular pore structures, the particulate matter is filtered and collected [8, 11, 12]. Depending on the filter geometry and mass flow rate (MFR), the pressure losses through the porous wall can contribute around 30% to 70% of the total pressure loss [13, 14]. Note that the clean filter pressure drop is a considerable part of the wall loss contribution [8, 13]. The clean-wall permeability is an important parameter characterising how easily gas passes through the filter wall; from it the pressure drop across the wall can be predicted as a function of through-wall gas velocity, temperature, and fluid viscosity. During operation, the pressure drop across the filter is affected by the presence of soot and ash, which may be present either as a separate layer lying on top of the filter wall and/or within the wall itself, altering its permeability. In either case, the knowledge of the clean-wall permeability is required for predicting backpressure across a soot- and/or ash-loaded filter. Moreover, in GPFs the soot layer is much thinner than it is in DPFs due to passive

regeneration, and therefore its contribution to the wall permeability is much less important [8].

To predict the flow losses through the porous wall, the well-established Darcy's Law [15] is usually used. The law applies to viscous laminar flow only; however, for higher velocity flows the non-linear Forchheimer extension [16] can be used to account for inertial effects. The law states that the pressure drop is inversely proportional to the permeability of the medium, k, therefore a correct estimate of the through-wall losses relies heavily on the value of k [6]. The wall permeability is property of the filter wall, and therefore, once known, can be used for the design of filters with different sizes and wall geometry. The clean filter wall permeability allows pressure drop across the filter wall to be predicted as a function of flow rate and temperature. Four of the most common methods for the estimation of k include experimental curve fitting, analytical expressions, wafer studies, and computational techniques.

Experimental curve fitting is the most common approach for permeability estimation. It involves fitting a linear or quadratic curve to experimental pressure drop data from full-size filters or cores to determine a suitable value for k, and, if included, the Forchheimer coefficient, β [5, 6, 17, 18, 19, 20]. However, there is a potential here to under/overestimate the k values due to the difficulty in isolating the through-wall losses from other contributions present when testing cores/full-size filters (e.g., frictional losses along the channels, contraction/expansion losses).

Without experimental data, an alternative method is to use analytical models to evaluate k [9, 21]. However, these are not very accurate when applied to filter wall media. This is evident from the comparison made by Sprouse et al. [21], where four commonly used expressions were shown to result in, at least, a 50% error in the overall backpressure prediction for filters. Most empirically derived expressions [22] were developed for packed beds of particles or fibres so for use with consolidated media, such as filter material, a level of error is induced. Common theoretically derived expressions [22] are based on conduit flow and therefore idealise the porous medium as a bundle of capillaries, thus reducing the accuracy. In addition, the analytical models are mostly a function of porosity and a characteristic dimension of the particle or the conduit. For filters, different definitions of the characteristic dimension are used [5], adding another layer of uncertainty.

Numerous published works have studied wafer sections cut from full-size filters [23, 24, 25, 26, 27]. In wafer experiments, only the through-wall losses are present, so the experiments can be used to understand the permeability properties and the effects of soot/ash loading. By measuring the pressure drop across a wafer sample and using Darcy's law, one can calculate the permeability with reasonable accuracy. In [24, 25, 26, 27] the focus is on the collection efficiency of a cordierite section representative of DPF channel walls. The wafer section is nearly 1mm in thickness, almost three times thicker than the wafers obtained from GPFs and those used in this study. Viswanathan et al. [24] and Wirojsakunchai et al. [25] use the same experimental setup, which has a contraction and expansion section before and after the wafer sample, thus adding a non-linear term to the pressure drop equation. This means the permeability and the contraction/expansion coefficient are calculated by curve fitting, introducing the same level of uncertainty present in core/full-size filter test data curve fitting. Wafers in [26] are used to study the impact of gas velocity on transient soot loading. Any estimation of permeability is not documented. Kamp et al. [27] investigate the effect of ash loading on the permeability of wafers by using image-based direct numerical simulation (DNS). The developed model predicted clean and ash-loaded wafer permeability within 20% of the measured values.

Other published works [28, 29, 30] have utilised imaging/tomography-based techniques to reconstruct a pore-scale 3D geometry for numerical simulations. A permeability can then be found by using the Darcy-Forchheimer law with simulated pressure drop results. The main drawback of this method is the experimental and computational expense in both the reconstruction and CFD (computational fluid dynamics) simulation. The model from Jaganathan et al. [28] has been developed for fibrous materials and shows a good agreement with fibrous analytical models and the narrow range of experimental data used. The model from Petrasch et al. [29] has been developed for a reticulate porous ceramic; however, its performance is not assessed against experimental data. The author uses the simulated value for k as the "exact" value, and a comparison with thirteen analytical models is made. Of those available to filter modellers, without knowledge of local pore properties, the Carman-Kozeny [22] model performs best but underpredicts values by 15.08%. The model from Kočí et al. [30] has been developed for coated automotive particulate filters. Using X-ray tomography, a 3D pore-scale reconstruction is created, and coupled with CFD to analyse the effects of a catalyst washcoat in, and on the channel walls, on the permeability and flow characteristics. The model presents a powerful tool for understanding macroscopic flow properties; however, without experimental validation, it can only be used qualitatively.

Most of the existing permeability measurements have been performed for cold flow [5, 6, 9]. However, at gas temperatures characteristic of exhaust systems, gas rarefication and thus the so-called slip-effect may become important. Aleksandrova et al. [23] utilised a hot flow rig to study the slip-effect. Darcy's law was used to find wafer permeability at different temperatures. It has been shown that the permeability increases by up to 30% at 450°C compared to the cold flow. While this effect is alluded to in some papers and models [6, 17, 19, 20], its influence is mostly neglected.

Due to the experimental, and computational expense of wafer or tomography-based estimation methods, it is no surprise that most backpressure prediction models opt for curve fitting or use analytical models when estimating k. The validity of these methods for automotive particulate filters has not been extensively assessed in the literature, and a comparison of different filter properties against these methods would give valuable insight into their performance for a wide range of applications.

Therefore, the present paper aims to use an experimental flow rig with wafer sections to establish a better understanding of the factors influencing filter wall permeability such as the medium and fluid properties. Using four different filters with different porous wall properties (porosity and mean pore size) the effect of these wall properties on the permeability is

investigated. This allows the popular k estimation methods and their validity for this application to be assessed. By measuring flow losses through filter wafers at different temperatures, the magnitude of the slip-effect for different filters is also estimated and is shown to vary with the wall properties. This is important for the prediction of through-wall losses in applications where permeability increase with temperature is a desirable effect. Understanding its magnitude and link to the filter properties will enable the development of more accurate models for filter design.

Methodology

Sample Preparation

To assess the effect of the substrate properties (porosity, pore size, wall thickness) on the permeability, the wafer samples for this study were taken from four different substrates made of two different materials with varying physical properties (Table 1). All four of the substrates used were uncoated, clean substrates, sourced directly from the manufacturer, and were thus clean/free of external impurities or channel blockages. Care has been taken during wafer and core sample preparation to minimise potential blockage of the pores (cutting performed next to an extractor fan).

Note that the values given in Table 1 are the nominal values provided by the manufacturers, and the substrates may have a range of Mean Pore Size (*MPS*) and porosity (ϵ) values throughout the part, as well as variations between different batches.

The test samples are rectangular-shaped wafers of one wall thickness (≈0.3mm) cut from full-size substrates using a piercing saw. After cutting, the wafers were sealed into sample holders consisting of high-temperature ceramic gaskets (Fig 1). A ring of copper silicon sealant was used on both sides of the wafer to ensure a seal and prevent movement in the sample holders across the range of temperatures tested. The open area of the wafer presented to the flow is circular and 50mm in diameter.

A key challenge during the sample preparation stage regards the ridges that were left on the wafer from the orthogonal walls (visible in Fig. 1). A flat metal blade was used to remove the ridges on one side of the wafer before cutting it from the substrate. Time and care were taken to cut as close to the wall as to reduce the height of the ridges remaining on the other side. While one side of the wafer was flat (the side where the ridges were removed), the other side still had some small visible ridges (Fig. 1). The height of the ridges varied between 0-2 wall thicknesses. Most attempts to remove them from a wafer already detached from a full-size substrate would end in the wafer cracking or breaking completely.

TABLE 1 Properties of substrates used in this study.

#	Material	Mean Pore Size (μm)	Porosity (%)	Wall Thickness (mm)
1	X	15	49	0.33
2	Y	18	65	0.305
3	X	17.5	59	0.305
4	Y	13	52	0.305

FIGURE 1 High-temperature ceramic sample holders and wafer sample.

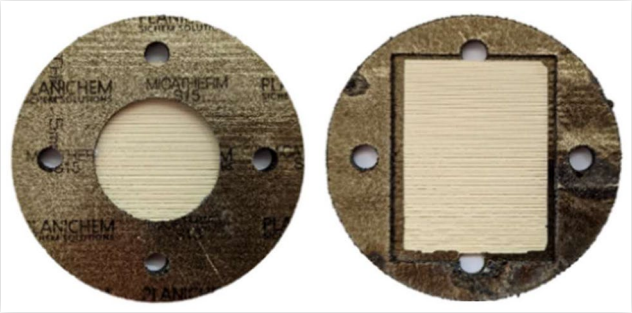

Experimental Setup

A flow rig (Fig. 2) incorporating a 32-kW electric heater was used for wafer testing. Depending on the design of the engine (e.g. displacement, fuel, etc.), the operating conditions, and the distance between the filter and the exhaust ports, the temperatures of exhaust gases in the filter can be anywhere between 250-900°C [31]. The maximum temperature through the wafer achieved in this study was 400°C.

As well as quite a broad range of temperatures, the flow rates through the filter wall during operation cover a wide range (0-0.6m/s) [31]. The setup used here can achieve mass flow rates up to 1g/s, corresponding to mean wall velocities

FIGURE 2 Schematic diagram of flow rig.

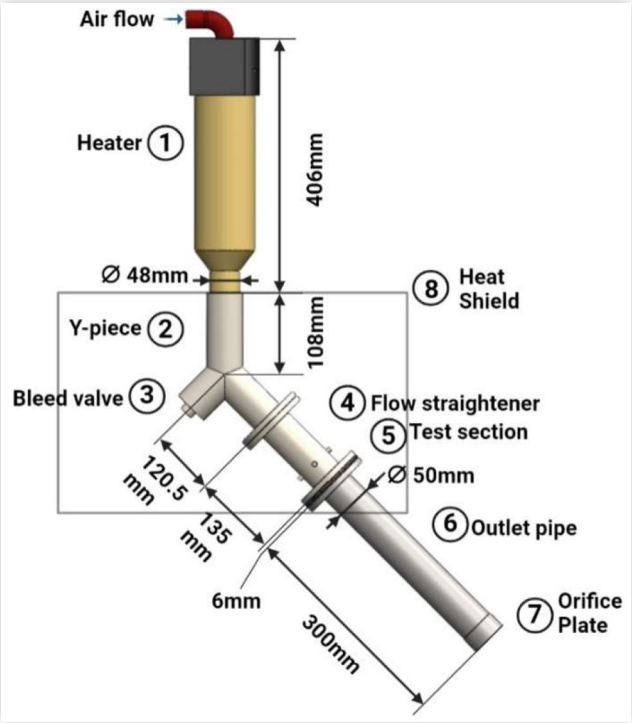

up to 0.5m/s at 25°C. The small mass flow rates through the wafers were achieved with a bleed valve upstream of the sample section (Fig. 2). An orifice plate with a Pitot tube was calibrated using a viscous flow meter (VFM), supplied with compressed air for reference. The VFM error is estimated to be around 3%-4% at MFR up to 10 g/s. The Pitot tube is used with a micromanometer of accuracy +/-0.25% of the reading and a resolution of 0.001 Pa.

The pressure differential across the wafer is measured with a digital manometer with an accuracy within 0.3% of the reading and a resolution of 1Pa using four pressure tappings spaced azimuthally around the pipe, 50mm upstream and downstream of the test section. For hot flow tests, two K-type thermocouples were positioned 32mm upstream and downstream of the wafer. Thermal equilibrium was considered achieved when temperature fluctuations were less than 1°C over the 5 minutes before measurements were recorded. To estimate the viscosity, density, and wall velocity at the wafer, the variation between upstream and downstream temperature values was assumed linear, and thus the average value was used. For cold flow the up/downstream temperature difference was negligible. However, for hot flow, the difference between upstream and downstream measurements was up to 40°C at 400°C.

Readings were sampled at a rate of 0.2s for 5 seconds and averaged for each measurement point.

Permeability Estimation

Using Darcy's law:

$$\Delta P = \frac{\mu}{k} w U_w, \tag{1}$$

one can determine permeability at each measurement point. Here, U_w is the superficial wall velocity (m/s), w is the thickness of the wall (m), ΔP is the pressure difference (Pa) across the wafer, and μ is the viscosity of the air (Pa.s) calculated using Sutherland's law [32]:

$$\mu = \mu_0 \left(\frac{T}{T_0} \right)^{\frac{3}{2}} \times \frac{T_0 + 110.4}{T + 110.4} \tag{2}$$

Here, $\mu_0 = 1.849 \times 10^{-5} Pa.s$ is the viscosity at $T_0 = 25°C$. T is the average temperature calculated from the upstream and downstream thermocouple measurements.

Results

Figure 3 shows the pressure drop against the mean superficial through-wall velocity at room temperature (≈25°C). As the substrate walls have different thicknesses, the pressure drop has been divided by the wall thickness, so the y-axis has units of Pa/mm. For each substrate, at least four wafer samples were used, and measurements were taken going up and down the flow rate range. The maximum deviation from the mean values is less than 12% for wall velocities above 0.15 m/s. At flow velocities below 0.15m/s, the error is higher due to the sensitivity of the manometers.

FIGURE 3 Cold flow test results comparing different substrates as well as results from [23].

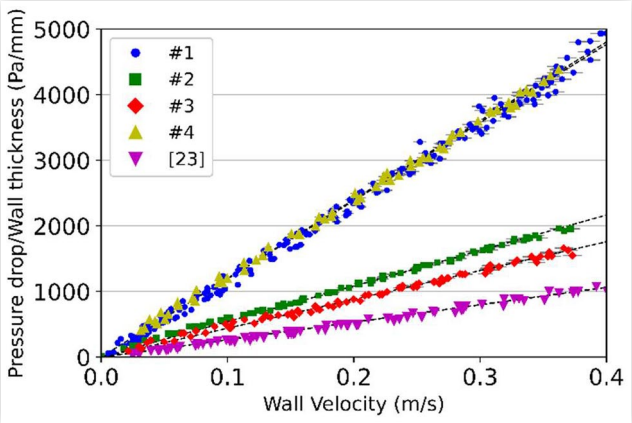

FIGURE 4 Permeability from cold flow tests for substrate #2.

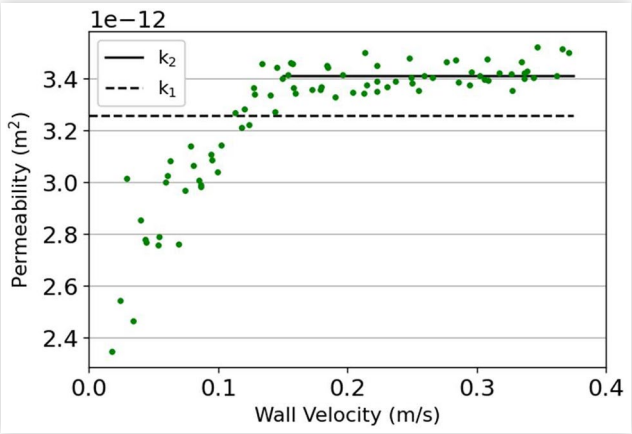

The four substrates used in this study are compared with the results in [23], where authors used a similar experimental setup and a single substrate made from cordierite.

Figure 4 shows the permeability calculated for each measurement point for substrate #2 using Eq. 1. The mean of these values gives a value for permeability, k_1. However, for wall velocities below 0.15m/s, the values of k are lower, while above that velocity the values seem to converge to a single value. This is attributed to the higher uncertainty of the measurement technique at low mass flow rates. For this reason, taking the average of the permeability for wall velocities above 0.15m/s yields a more representative permeability k_2. While Figure 4 shows data for substrate #2 only, a similar trend was observed for all substrates (Fig. 5).

Figure 5 shows the permeability at all points for all substrates divided by their corresponding k_2 value. It is clear for all substrates that for wall velocities above 0.15m/s, there is convergence to the k_2 value. Therefore, in the rest of this study the k_2 value, which differs from k_1 by around 5%, is used.

The cold flow permeability measured for each substrate is tabulated below:

TABLE 2 Cold flow permeability values for substrates in this study.

Substrate #	Permeability (m^2)
1	1.53×10^{-12}
2	3.41×10^{-12}
3	4.18×10^{-12}
4	1.54×10^{-12}

FIGURE 5 Permeability divided by k_2 for all substrates.

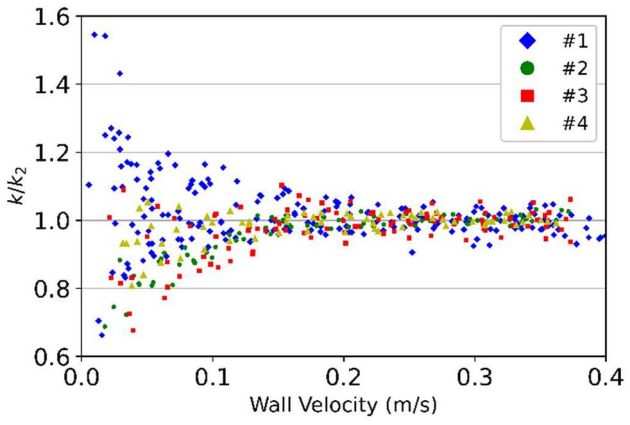

An important observation from Fig. 3 is the linearity of the plot. This suggests that the Forchheimer losses are negligible for the parameters and substrates used in these tests. As an additional indicator, Dullien [22] suggests a pore Reynolds number (Eq. 3) of less than 1 indicates laminar flow and negligible Forchheimer effects:

$$Re_p = \frac{U_w \sqrt{k}}{\nu} \tag{3}$$

Here, ν is the kinematic viscosity (μ/ρ).

In the current study, the maximum value for Re_p is approximately 0.03, confirming that the flow is laminar, as well as the validity of Darcy's law and negligible inertial effects.

Effect of Ridges

The influence of the ridges on the accuracy of permeability measurements has been investigated numerically in [23], where it has been suggested that the flow contracts and enters the ridges at the side. A correction factor (Eq. 4) was suggested, which adjusted the permeability by up to 10%.

$$k = \frac{a\mu}{2\Delta P} U_w \times \left[\frac{d_h}{2w} + \frac{1}{\pi} ln\left(1 + \frac{\pi}{2}\right) \right]^{-1} \tag{4}$$

Here, a is the cell pitch, and d_h is the hydraulic diameter of the channel.

However, the study [23] only considered one type of uncoated monolith, and thus care should be taken in extrapolating the results to monoliths with different properties and permeabilities. To investigate this further, two additional types of samples were tested. The first set was prepared as above to reduce the height of the ridges, while the second set was prepared to leave the ridges on the wafer (see Fig. 6).

Due to time limitations only substrates #1 and #4 were tested in the ridges study.

Figure 7 shows the results from the tests for substrate #4 for ridged, clean, and normally prepared wafer samples. Each sample was tested twice alternating the side of the wafer presented to the flow. For this substrate, it was found that the variation in results was similar in magnitude (less than 5%) to the spread of data for normally prepared wafers. The ridged and clean wafers performed the same as the normally prepared wafers, and thus the effect of the ridges could be ignored. Figure 8 depicts similar results for substrate #1 which again shows no clear correlation that the ridged or clean wafers behave differently beyond the variation found in the normally prepared wafers (less than 8%). It is estimated for a large variation in the data, up to 10%, there can be around a 4.5% effect on the permeability determined and thus, the effect of the ridges can be mitigated by testing a larger number of wafers from each substrate (prepared normally) and taking the average.

FIGURE 6 Ridged wafers (A and B) and clean wafers (C and D).

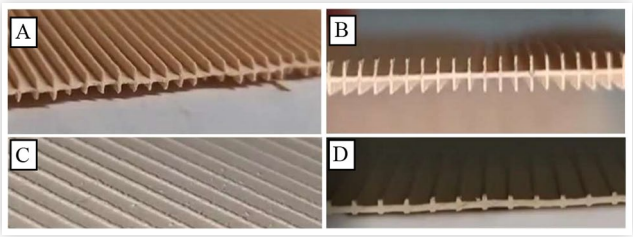

FIGURE 7 Pressure drop results from ridges study for substrate #4.

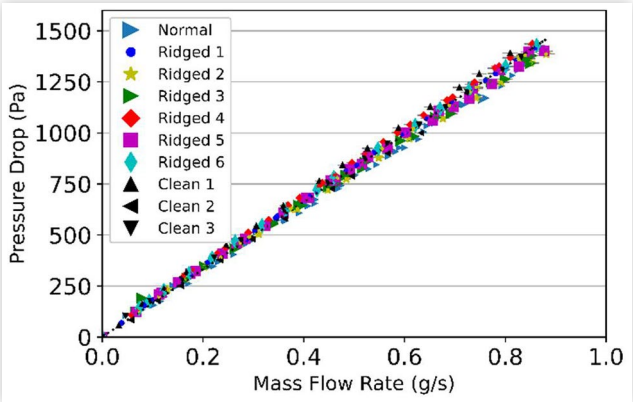

FIGURE 8 Pressure drop results from ridges study for substrate #1.

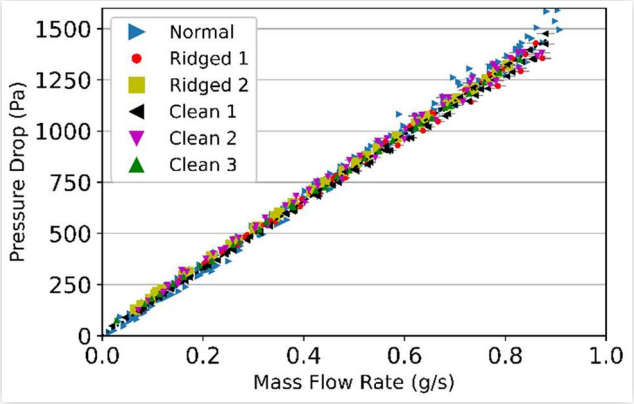

Comparison with Permeability Derived from Core Testing

A common method to calculate a value of k is by fitting the model to experimental data from cores or full-size filters [5, 6, 17, 18, 19, 20]. For example, Konstandopoulos et al. [6, 8] use the experimental data from pressure drop measurements from a full-size particulate filter flowed with air at room temperature. To investigate the accuracy of this method the flow rig was adapted to measure the pressure drop across 50mm diameter cores cut from full-size filters. Only substrates #2 and #3 were chosen for this study due to time limitations. The experimental results were then used to estimate a permeability which is compared with the values obtained from wafer measurements.

Two approaches are used here. In the first approach, both frictional and contraction/expansion losses are assumed to be known. The frictional losses are estimated from Eq. 5, and contraction/expansion losses are estimated from Eq. 6:

$$\Delta P_{friction} = \frac{2\mu FL}{3d_h^2} U \tag{5}$$

$$\Delta P_{contr/expan} = \zeta \frac{\rho}{2} U^2 \tag{6}$$

Here, U is the mean velocity at the inlet channel entrance, μ is the viscosity calculated using Sutherland's Law (Eq. 2), F = 28.454 is the viscous loss coefficient for a square cross-section duct (see [33]), L is the length of the core, d_h is the cell hydraulic diameter, and ζ is the contraction/expansion coefficient calculated using the Borda-Carnot equation [34]:

$$\zeta_{contr} = 0.5\left(1 - \frac{A_1}{A_2}\right) \tag{7}$$

$$\zeta_{exp} = \left(1 - \frac{A_1}{A_2}\right)^2 \tag{8}$$

Note that Eq. 5 approximates the one-dimensional pressure loss model derived in [8].

These estimates are subtracted from the total pressure drop to give $\Delta P'$:

$$\Delta P' = \Delta P_{core} - \Delta P_{friction} - \Delta P_{contr} - \Delta P_{expan} \tag{9}$$

Then linear fitting is used to determine k:

$$\Delta P' = \alpha U \quad \rightarrow k = \frac{\mu}{\alpha}\frac{d_h w}{4L} \tag{10}$$

In the second approach, only the frictional losses defined by Eq. 5 are subtracted from the total pressure drop to give $\Delta P''$:

$$\Delta P'' = \Delta P_{core} - \Delta P_{friction} \tag{11}$$

A quadratic curve with two coefficients α and β is fitted to the resulting pressure drop, and used to derive a permeability, k, and a single inertial coefficient, ζ, representing the contraction and expansion losses upstream and downstream of the filter channels:

$$\Delta P'' = \alpha U + \beta U^2 \quad \rightarrow \zeta = \frac{2\beta}{\rho} \tag{12}$$

Figure 9 shows the linear fit of the core data from both substrates. To ensure that any inertial effects were negligible, the fitting was done at the lower velocity range (up to a channel Reynolds number, $Re = \rho U d_h/\mu$, of around 700). The estimated permeability for substrate #3 (Table 3) is 26 times smaller than the value measured with wafers. For substrate #2 the value is around 13 times smaller.

FIGURE 9 Curve fitting to obtain k from core data for substrates #2 and #3 using linear fitting.

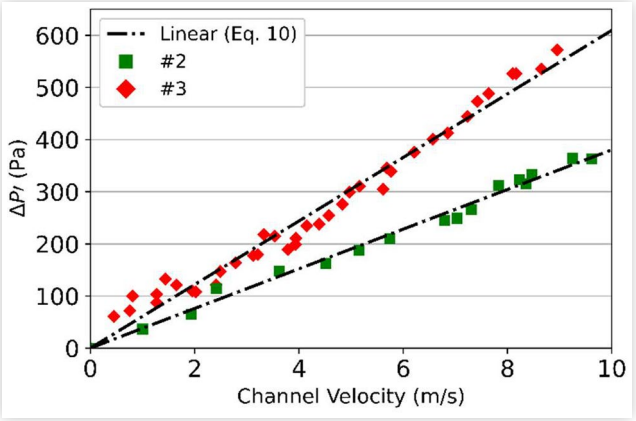

TABLE 3 Comparison of permeability and inertial coefficient derived from core data with measured permeability from wafers.

Substrate	#2		#3	
	k (m^2)	ζ	k (m^2)	ζ
Wafers	3.41×10^{-12}	-	4.18×10^{-12}	-
Linear	2.63×10^{-13}	-	1.62×10^{-13}	-
Quadratic	7.13×10^{-13}	6.4	3.19×10^{-13}	9.02

For $\Delta P''$ a quadratic curve mostly captures the pressure drop trend (Fig 10) and provides more accurate results when compared with the permeability measured with wafers. However, there is still considerable error. For Substrate #2 this error was about 52%, while for substrate #3 the predicted value was out by over one order of magnitude.

As discussed in the introduction, the difference between the predicted permeability values from cores and wafers is attributed to the accumulation of uncertainties from the estimation of frictional and inertial pressure losses in core testing. The linear fitting of pressure drop data (Fig. 9) assumes that all inertial losses come from contraction and expansion, and that these losses can be reliably estimated using Borda-Carnot or a similar expression. However, there is no single accurate expression for contraction/expansion losses in the laminar regime [13]. Moreover, there is likely to be a non-linear coupling between the different pressure loss contributions. This is confirmed by the fact that using quadratic fitting results in different values for the inertial coefficient depending on the Reynolds number range used for fitting. For example, using a Reynolds number up to 2000 gives $\zeta = 7.23$, while using a Reynolds number up to 1000 gives $\zeta = 4.77$. If only contraction/expansion losses were responsible for the inertial effects, these coefficients should be closer in magnitude.

Due to the larger contribution of the frictional losses compared to the inertial losses, the accuracy of the friction loss model is even more important. The model used here (Eq. 5) is adopted from [8] and is based on several assumptions that may or may not be valid for the current configuration. Additionally, it assumes the pressure loss contributions can be de-coupled.

Finally, the core fitting method assumes that the flow and pressure losses are the same in all the filter channels. This does not account for variations throughout the filter of channel geometry, plug length, or blocked channels on the periphery of the core.

In summary, the core testing method relies heavily on several assumptions and parameters. Eliminating these by testing wafer samples results in increased accuracy of the permeability predictions – potentially by an order of magnitude (Table 3). According to the core testing results, substrate #2 has a higher permeability than substrate #3. However, the results from wafer testing and trends from existing correlations (see Fig. 11) suggest that substrate #3 should be the more permeable of the two.

FIGURE 10 Curve fitting to obtain k from core data for substrates #2 and #3 using quadratic fitting.

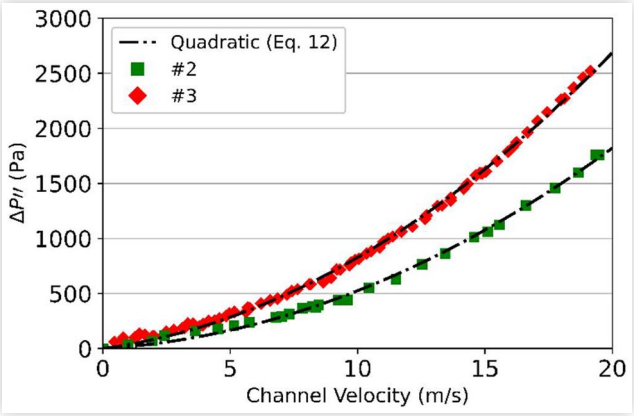

FIGURE 11 Non-dimensional measured permeability vs porosity with analytical expressions Eqs. (13-16).

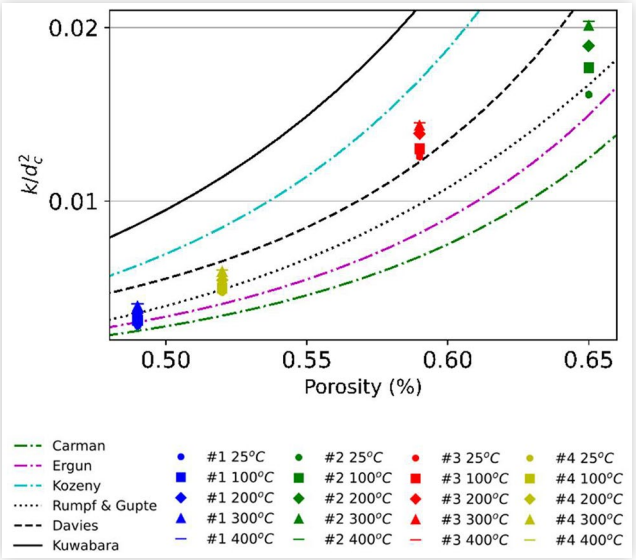

Comparison with Permeability Estimations from Analytical Models

The literature surrounding flow through porous media is vast due to its applicability in many industries. A range of analytical models for permeability estimation have been proposed by numerous authors for various applications. The most common ones are discussed here.

The model which often gets the most attention is the theoretically derived Kozeny-Carman equation [35, 36]. It relies on a few assumptions. Firstly, the porous medium is made up of conduits that can be complex in cross-section but have, on average, a constant area. The flow through the conduits is laminar and can be described by a modified Poiseuille's equation using the 'hydraulic radius' to generalize the bulk flow through the medium. Upon comparison with Darcy's law, k can be expressed in terms of the hydraulic radius, R_H. The final assumption is for the computation of R_H. Carman considered beds of packed spheres and expressed k in terms of the porosity, ϵ, and the sphere/particle diameter, d_p:

$$k = \frac{\epsilon^3}{k_k\left(1-\epsilon\right)^2} d_p^2 \tag{13}$$

Here, k_k is termed the 'Kozeny constant' and for uniform spherical particles is equal to 72. In Carman's later work [37] this value was adjusted based on experimental data, to 180, and again by Ergun [38] to 150. Due to the limitations of packed beds of spheres, many authors have since suggested values or corrections for k_k based on the experimental data from a plethora of porous materials. A review of these can

be found in [39] where it is clear the range is considerably wide (54 - 180).

The next two models are empirically derived. Rumpf & Gupte [40] proposed a correlation (Eq. 14) based on experiments with packed beds of spherical particles of various sizes. A relatively wide porosity range of 35% to 70% is achieved using monodispersed spherical particles.

$$k_{Rumpf} = \frac{\epsilon^{5.5}}{5.6}\bar{D}_{p2}^2 \tag{14}$$

Here, $\bar{D}_{p2}$ is the diameter of the spheres with average surface area.

In contrast to the above models, the model proposed by Davies et al. [22] was calibrated for fibrous packed beds which are, arguably, more akin to filter material than particle beds:

$$k_{Davies} = \frac{d_f^2}{64\left(1-\epsilon\right)^{\frac{3}{2}}\left(1+56\left(1-\epsilon\right)^3\right)} \tag{15}$$

Here d_f is the diameter of a fibre.

The final model considered here was proposed by Kuwabara et al. [42]. Using Stokes' law the medium is considered to consist of randomly parallel-arranged cylinders or spheres and the permeability is expressed as:

$$k_{Kuwa} = \frac{2}{9}\times\frac{2-1.8\left(1-\epsilon\right)^{\frac{1}{3}}-\epsilon-0.2\left(1-\epsilon\right)^2}{1-\epsilon}l_{ch}^2 \tag{16}$$

Here, l_{ch} is the characteristic length scale which presents a common problem when applying any of these models to filters. The expression has been tested up to a porosity of 84% and is shown to perform well.

For unconsolidated media, such as packed spheres, or cylinder and sphere arrangements, the characteristic dimensions (d_p, d_f, l_{ch}) are known, and perhaps controlled. For consolidated media (such as filters) they are not, and estimating this dimension is error-inducing. In most automotive applications, only the mean pore size is readily available. Dullien [22] suggests using the characteristic dimension of a spherical collector, d_c, defined as:

$$d_c = \frac{3\left(1-\epsilon\right)}{2\epsilon}MPS \tag{17}$$

Note, the factor of $3(1-\epsilon)/2\epsilon$ is equal to 1 when ϵ is equal to 0.6. For the porosities of the substrates considered in this study (see Table 1), the difference between the mean pore size and the spherical collector diameter varies between 19% and 56%, therefore it is important to use the correct length for each model used.

To assess the performance of the correlations the non-dimensional permeability, k/d_c^2, is plotted vs porosity in Figure 11 and compared with the experimental results. Despite the many assumptions and idealisations at the core of these models, the Rumpf & Gupte model (Eq. 14) performs reasonably well for the substrates with material 'Y' (#2 and #4) with less than 4% error for cold flow. The largest error for this model, at cold flow, is for substrates #1 and #3 (material 'X') which is around 25%. This suggests that material structure and pore distribution are key parameters, and that porosity and mean pore size alone may be insufficient for an accurate estimate of permeability for all filter materials.

It is interesting to note, the best performing correlations here are those derived empirically. For example, even the Kozeny-Carman equation (Eq. 13) performs best with the Kozeny constant, k_k=72, adjusted based on experiments (to 150 by Ergun [38] and to 180 by Carman [37]).

The values of permeability calculated with the methods documented in this study are tabulated in Table 4. The model that performs the best when compared with the wafer measurements is the Rumpf & Gupte model (Eq. 14); however, for substrate #3, the error is still around 25%.

The associated error with both methods (analytical models/Core testing) are attributed to the accumulation of assumptions and simplification of the problem. Analytical models fail to capture the complexity of the flow physics and pore structures while the core testing method assumes the individual contributions to the pressure drop can be de-coupled.

Hot Flow Tests

Another observation from Figure 11 is the spread of permeabilities for different gas temperatures, suggesting temperature may also play a key role. Since the Darcy pressure losses (Eq. 1) increase linearly with the wall velocity, the total measured pressure drop will increase with temperature for a fixed mass flow rate.

Non-dimensionalising these results using the Reynolds number and the dynamic pressure yields Figure 12. Here, the Reynolds number is defined using the wafer diameter as the length scale (50mm). The curves do not coincide, suggesting that the difference is due to another non-dimensional group dependent on temperature.

Using the same approach as described for the cold flow to calculate the permeability, one can compare permeability

TABLE 4 Comparison of cold flow permeability values estimated using methods documented in this study.

	Permeability, k (m^2)			
	Substrates			
	1	2	3	4
Experiments				
Wafer Tests	1.53×10^{-12}	3.41×10^{-12}	4.18×10^{-12}	1.54×10^{-12}
Core Testing method - Linear	-	2.63×10^{-13}	1.62×10^{-13}	-
Core Testing method - Quadratic	-	7.13×10^{-13}	3.19×10^{-13}	-
Analytical models				
Rumpf & Gupte [40]	1.94×10^{-12}	3.53×10^{-12}	3.26×10^{-12}	1.59×10^{-12}
Davies [22]	1.55×10^{-12}	2.04×10^{-12}	1.96×10^{-12}	1.13×10^{-12}
Kozeny [35]	1.38×10^{-12}	2.63×10^{-12}	2.26×10^{-12}	1.10×10^{-12}
Carman [37]	3.45×10^{-12}	6.58×10^{-12}	5.65×10^{-12}	2.74×10^{-12}
Ergun [38]	1.65×10^{-12}	3.16×10^{-12}	2.71×10^{-12}	1.32×10^{-12}

FIGURE 12 Non-dimensional pressure drop vs Reynolds number for substrate #1.

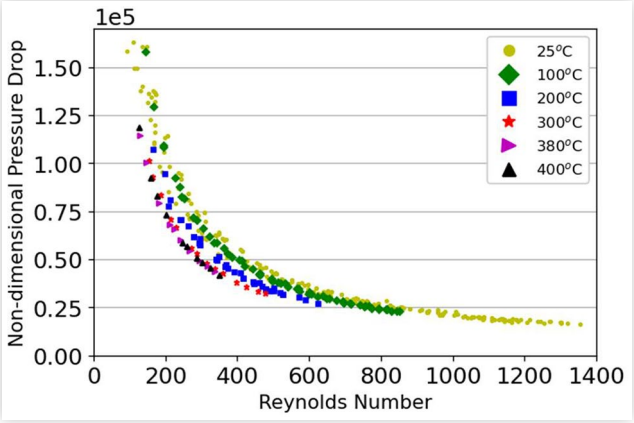

for different temperatures for all substrates. In Figure 13 the permeability is divided by the value of k for cold flow (around 25°C) for each substrate, respectively. The results show that the permeability increases with temperature by at least 15% at 400°C for all substrates and by around 45% for substrate #1. These results are consistent with those found in [23].

A possible explanation for this is the effect of slip at the pore walls. If the mean free path length of the gas molecules becomes comparable with the size of the pore, the velocity at the wall has a finite value and thus the no-slip condition fails [22].

The slip-effect can be characterised using the Knudsen number (Kn), a dimensionless number defined as the ratio of the molecule's mean free path length (λ) to a representative physical length scale (D):

$$Kn = \frac{\lambda}{D} \tag{18}$$

The molecular mean free path, λ, is calculated with Eq. 19 which involves known parameters including Boltzmann's constant, k_B, temperature, pressure, and σ^2, which is the collision diameter defined by Eq. 20:

$$\lambda = \frac{k_B T}{\sqrt{2}\pi\sigma^2 P} \tag{19}$$

FIGURE 13 Scaled permeability (k/k_{cold}) vs temperature.

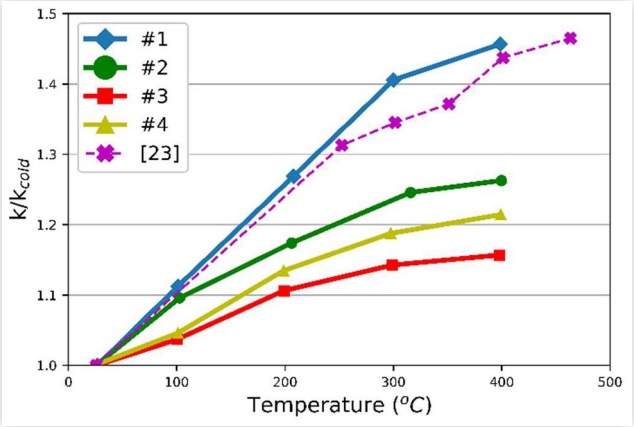

$$\sigma^2 = \frac{2\sqrt{mk_B T}}{3\pi^{\frac{3}{2}}\mu} \tag{20}$$

Here, m is the molecular mass of air (m = 28.971/NA (g) with NA = 6.022×10^{-23}).

The length scale, D, in Eq. 18 is defined differently by different authors. In Knudsen's original work [43] the radius of a tube was used as the characteristic dimension. For filters, the spherical collector radius, $d_c/2$, with d_c defined in Eq 17, is used in this study and others [4, 6, 14, 17, 23].

For Knudsen numbers higher than 0.01 the flow through the porous medium is expected to experience the slip-effect [23]. However, it should be noted that this has an element of uncertainty and can thus be used qualitatively rather than quantitatively. Plotting permeability against the Knudsen number for all substrates (Fig. 14) shows that with this definition the Knudsen number goes above 0.01, and thus the slip flow regime should be considered. It is also noticeable that even for cold flow which corresponds to the lowest Knudsen numbers, there may still be some level of slip-effect.

Scaling the permeability values for different substrates using the expression:

$$K = \frac{k}{k_0} - 1, \tag{21}$$

allows us to compare the importance of the slip effects for the four substrates (Fig. 15). Using linear regression, the values for k were extrapolated to Kn = 0 to find the no-slip permeability, k_0.

Substrates #2, #3, and #4 have a similar permeability slope for the range of Knudsen numbers considered. Substrate #1 experiences much higher permeability variation with the Knudsen number. Although substrate #1 has thicker walls, it is not clear if this could affect the slip properties of the walls. The reason for different magnitude of the observed slip effect will be further investigated in a future study.

Several predictive models exist to describe the wall permeability at higher values of the Knudsen number. Figure 16-19 compares the three different models (Eqs. 22-24 below) with the measured results from the experiments.

FIGURE 14 Non-dimensional permeability vs Knudsen number for all substrates.

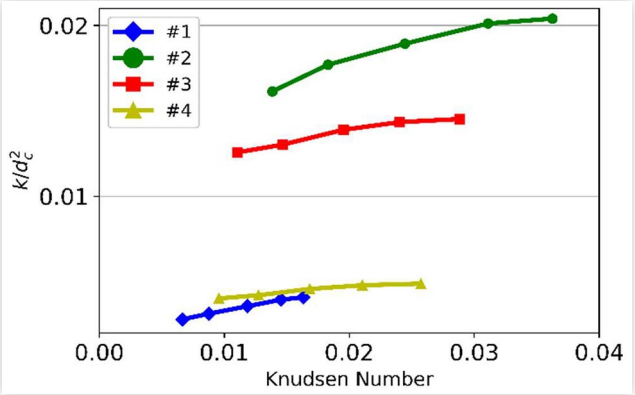

FIGURE 15 Scaled permeability $(k/k_0) - 1$ vs Knudsen number for all substrates.

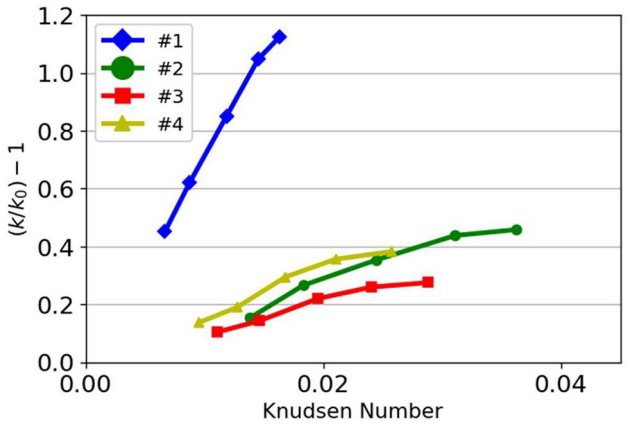

FIGURE 16 Scaled permeability $(k/k_0) - 1$ vs Knudsen number for substrate #1 comparison with slip-effect models.

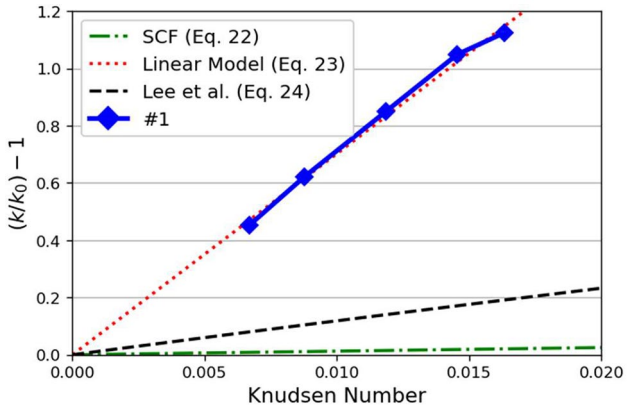

FIGURE 17 Scaled permeability $(k/k_0) - 1$ vs Knudsen number for substrate #2 comparison with slip-effect models.

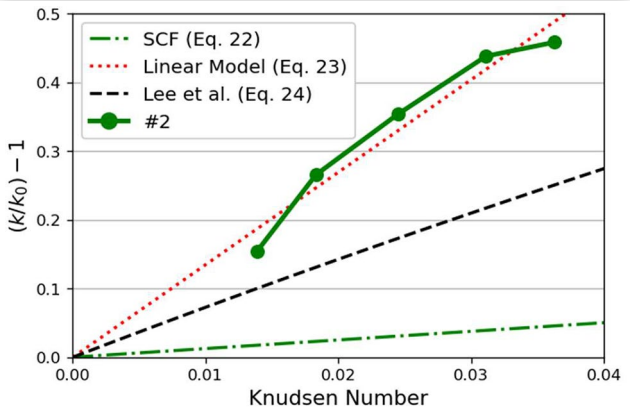

Using the Stokes-Cunningham Factor as in [8]:

$$\frac{k}{k_0} = SCF = 1 + Kn\left(1.257 + 0.4e^{\frac{-1.1}{Kn}}\right) \tag{22}$$

FIGURE 18 Scaled permeability $(k/k_0) - 1$ vs Knudsen number for substrate #3 comparison with slip-effect models.

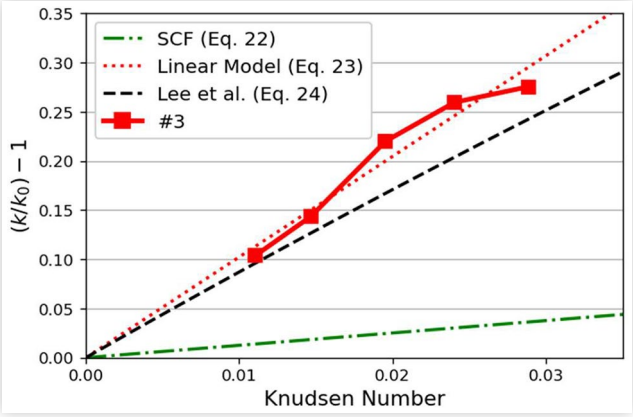

FIGURE 19 Scaled permeability $(k/k_0) - 1$ vs Knudsen number for substrate #4 comparison with slip-effect models.

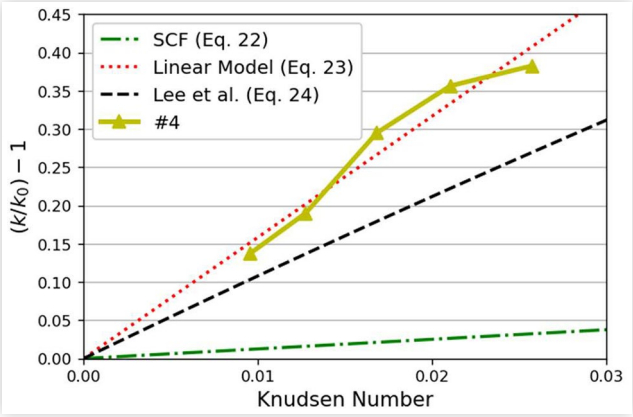

Maxwell et al. [44] suggest a linear fitting is sufficient with the calibration of the coefficient C_1 to experimental data (used for filters in [23]):

$$\frac{k}{k_0} - 1 = 4C_1 Kn \tag{23}$$

Lee et al. [45] suggested a model using the tangential momentum accommodation coefficient, σ_v:

$$k = \frac{2\left(K_1 + 3K_2\sigma_v Kn\right)}{9\left(1-\epsilon\right)\left(1+2\sigma_v Kn\right)}\frac{d_c^2}{4} \tag{24}$$

Here, σ_v is equal to 1, and K_1 and K_2 are defined by the following:

$$K_1 = 2 - 1.8\left(1-\epsilon\right)^{\frac{1}{3}} - \epsilon - 0.2\left(1-\epsilon\right)^2 \tag{25}$$

$$K_2 = 1 - 1.2\left(1-\epsilon\right)^{\frac{1}{3}} + 0.2\left(1-\epsilon\right)^2 \tag{26}$$

From Figures 16-19, we can see that the SCF model [8] under-predicts the trend considerably for all substrates. The

TABLE 5 Values of C_1 for substrates used in [23] and this study.

Substrate #	C_1
1	17.57
2	3.37
3	2.56
4	3.96
[23]	11.14

model from Lee et al. also considerably under-predicts the change for substrates #1 and #2; however, is closer to the experimental results for substrates #3 and #4. The Maxwell model used in [44, 23] is only accurate because the constant, C_1, is found by fitting Eq. 23 to the experimental data. A study of a wider range of substrates is needed to establish if values of C_1 can be used for substrates with similar properties. The calculated values for C_1 using the experimental data from all four substrates used in this study, together with that found in [23], are listed in Table 5. The variation in the values suggests that the slip-effect magnitude does not solely depend on the filter material or the intrinsic properties. Substrate #2 is similar to that used in [23]; however, the corresponding value of C_1 is different by more than a factor of three. For this reason, it is difficult to suggest a narrow range or a value for C_1 that might fit all tested substrates. On the other hand, substrates #2 and #4 have the same material and values for C_1 within 16% of each other.

Conclusions

In this study, a robust and repeatable methodology has been demonstrated to allow for the measurement of the pressure drop across a section of channel wall found in automotive particulate filters. The results are used to estimate the permeability for both cold and hot flow, which is a key parameter influencing filter backpressure.

In this study the experimentally determined permeability for four different clean substrates has been compared with the analytical and empirical expressions developed for beds of packed spheres, arrangements of spheres and cylinders, and fibres. The results show that although for some of the substrates, the permeability estimates by these models were within an acceptable range (less than 15% difference), none of the existing expressions fully describe the permeability variation with substrate porosity and pore size. This suggests that other porous wall properties (e.g., tortuosity) need to be considered to produce accurate permeability predictions for different substrates.

The measurement method results have also been compared with the commonly used core test data analysis method, which involves using curve fitting to the experimental data to determine permeability and contraction/expansion coefficients. For the two substrates tested here (#2 and #3), the permeability values obtained from core testing differed from the measured values by at least one order of magnitude. The inability to separate frictional, inertial, and through-wall losses in core testing is the most likely reason for the error associated with the core testing method.

With increasing temperature, the permeability is known to increase due to the slip-effect. For temperatures up to 400°C used in this study, permeability increases by between 15% and 45%. Substrate #1 exhibited a much more pronounced slip effect than substrates #2-#4, which needs to be explained and will be the subject of future study. For substrates #2-#4, the permeability increase with the Knudsen number was of the same order of magnitude. In all cases, all the predictive slip-effect models considered underestimated the slip effect. For filters, this is a welcome result, as an increase in permeability means a decrease in the additional backpressure generated. Moreover, with typical exhaust gas temperatures up to 900°C, the slip-effect may have an even greater contribution. This is something that can be investigated further with higher temperatures.

Although the method has been applied to clean, bare substrates, the clean filter permeability can be used for establishing pressure losses in coated and/or ash/soot loaded substrates, using the effective permeability [9]. The experimental method presented here can also be used to directly determine the permeability of coated or loaded wafers, which is the subject of a separate on-going study.

References

1. European Commission, "Commission proposes new Euro 7 standards to reduce pollutant emissions from vehicles and improve air quality," https://ec.europa.eu/commission/presscorner/detail/en/ip_22_6495m, accessed April 2023.
2. Johnson, T., "Vehicular Emissions in Review," *SAE Int. J. Engines* 9, no. 2 (2016): 1258-1275, https://doi.org/10.4271/2016-01-0919.
3. Guan, B., Zhan, R., Lin, H., and Huang, Z., "Review of the State-of-the-Art of Exhaust Particulate Filter Technology in Internal Combustion Engines," *J. Environ. Man.* 154 (2015): 225-258, doi:10.1016/j.jenvman.2015.02.027.
4. Koltsakis, G., Onoufrios, H., Depcik, C., and Ragone, J.C., "Catalyzed Diesel Particulate Filter Modelling," *Rev. Chem. Eng.* 29, no. 1 (2013): 161, doi:10.1515/revce-2012-0008.
5. Lambert, C., Chanko, T., Dobson, D., Liu, X. et al., "Gasoline Particle Filter Development," *Emiss. Control Sci. Tech.* 3 (2017): 105-111, doi:10.1007/s40825-016-0055-x.
6. Konstandopoulos, A., "Flow Resistance Descriptors for Diesel Particulate Filters: Definitions, Measurements and Testing," SAE Technical Paper 2003-01-0846, 2003, https://doi.org/10.4271/2003-01-0846.
7. DieselNet, "Engine Exhaust Back Pressure," https://dieselnet.com/tech/diesel_exh_pres.php, accessed Jan. 2023.
8. Konstandopoulos, A. and Johnson, J., "Wall-Flow Diesel Particulate Filters—Their Pressure Drop and Collection Efficiency," SAE Technical Paper 890405, 1989, https://doi.org/10.4271/890405.
9. Masoudi, M., Heibel, A., and Then, P., "Predicting Pressure Drop of Wall-Flow Diesel Particulate Filters - Theory and

Experiment," SAE Technical Paper 2000-01-0184, 2000, https://doi.org/10.4271/2000-01-0184.

10. Swanson, J., Watts, W., Kittelson, D., Newman, R. et al., "Filtration Efficiency and Pressure Drop of Miniature Diesel Particulate Filters," *Aerosol Sci. Tech.* 47, no. 4 (2013): 452-461, doi:10.1080/02786826.2012.763087.
11. Miller, P.R., Scoll, J., Bagley, S., Leddy, D. et al., "The Effects of a Porous Ceramic Particulate Trap on the Physical, Chemical and Biological Character of Diesel Particulate Emissions," SAE Technical Paper 830457, 1983, https://doi.org/10.4271/830457.
12. Rubino, L., Thier, D., Schumann, T., Guettler, S. et al., "Fundamental Study of GPF Performance on Soot and Ash Accumulation over Artemis Urban and Motorway Cycles - Comparison of Engine Bench Results with GPF Durability Study on Road," SAE Technical Paper 2017-24-0127, 2017, https://doi.org/10.4271/2017-24-0127.
13. Konstandopoulos, A.G., Skaperdas, E., and Masoudi, M., "Inertial Contributions to the Pressure Drop of Diesel Particulate Filters," SAE Technical Paper 2001-01-0909, 2001, https://doi.org/10.4271/2001-01-0909.
14. Haralampous, O.A., Kandylas, I.P., Koltsakis, G.C., and Samaras, Z.C., "Diesel Particulate Filter Pressure Drop Part 1: Modelling and Experimental Validation," *Int. J. Eng. Res* 5, no. 2 (2004): 149-162, doi:10.1243/146808704773564550.
15. Darcy, H., "Les fontaines publiques de la ville de Dijon," (Paris, Victor Dalmont, 1856), 570, https://books.google.co.uk/books?id=DOwbgyt_MzQC&pg=PA1&redir_esc=y#v=onepage&q&f=false, accessed Feb 2023.
16. Forchheimer, P., "Wasserbewegung Durch Boden," *Zeitschrift des Vereines Deutscher Ingenieure* 45 (1901): 1781-1788.
17. Aleksandrova, S., Saul, J., Prantoni, M., Medina, H. et al., "Turbulent Flow Pressure Losses in Gasoline Particulate Filters," *SAE Int. J. Eng.* 12, no. 4 (2019): 455-470, doi:10.4271/03-12-04-0030.
18. Liu, X., Kim, J., Chanko, T., Lambert, C. et al., "A Modeling Analysis of Fibrous Media for Gasoline Particulate Filters," SAE Technical Paper 2017-01-0967, 2017, https://doi.org/10.4271/2017-01-0967.
19. Prantoni, M., Aleksandrova, S., Medina, H., Saul, J. et al., "Modelling Pressure Losses in Gasoline Particulate Filters in High Flow Regimes and Temperatures," SAE Technical Paper 2019-01-2330, 2019, https://doi.org/10.4271/2019-01-2330.
20. Watling, T., Ravenscroft, M., Cleeton, J., Rees, I. et al., "Development of a Particulate Filter Model for the Prediction of Backpressure: Improved Momentum Balance and Entrance and Exit Effect Equations," *SAE Int. J. Eng.* 10, no. 4 (2017): 1765-1794, https://doi.org/10.4271/2017-01-0974.
21. Sprouse, E.C. III, Magnus, D.M., and Depcik, D.C., "Diesel Particulate Filter Model With Detailed Permeability Analysis," *IMECE2011-63687* , no. 1589 (2011): 1596, doi:10.1115/IMECE2011-63687.
22. Dullien, F.A.L., *Porous Media: Fluid Transport and Pore Structure* (New York: Academic Press, 1979), ISBN:978-0-12-223651-8.
23. Aleksandrova, S., Saul, J., Medina, H., Garcia-Afonso, O. et al., "Gasoline Particulate Filter Wall Permeability Testing," *SAE Int. J. Engines* 11, no. 5 (2018): 571-584, doi:10.4271/03-11-05-0039.
24. Viswanathan, S., Rothamer, D., Zelenyuk, A., Stewart, M. et al., "Experimental Investigation of the Effect of Inlet Particle Properties on the Capture Efficiency in an Exhaust Particulate Filter," *J. Aerosol Sci.* 113 (2017): 250-264, doi:10.1016/j.jaerosci.2017.08.002.
25. Wirojsakunchai, E., Kolodziej, C., Yapaulo, R., and Foster, D., "Development of the Diesel Exhaust Filtration Analysis System (DEFA)," *SAE Int. J. Fuels Lubr* 1, no. 1 (2009): 265-273, https://doi.org/10.4271/2008-01-0486.
26. Yapaulo, R.A., Wirojsakunchai, E., Orita, T., Foster, D.E. et al., "Impact of Filtration Velocities and Particulate Matter Characteristics on Diesel Particulate Filter Wall Loading," *Int J. Eng. Res.* 10, no. 5 (2009): 287-304, doi:10.1243/14680874JER0350.
27. Kamp, C., Zhang, S., Bagi, S., Wong, V. et al., "Ash Permeability Determination in the Diesel Particulate Filter from Ultra-High Resolution 3D X-Ray Imaging and Image-Based Direct Numerical Simulations," *SAE Int. J. Fuels Lubr.* 10, no. 2 (2017): 608-618, https://doi.org/10.4271/2017-01-0927.
28. Jaganathan, S., Vahedi Tafreshi, H., and Pourdeyhimi, B., "A Realistic Approach for Modeling Permeability of Fibrous Media: 3-D Imaging Coupled with CFD Simulation," *Che. Eng. Sci.* 63, no. 1 (2008): 244-252, doi:10.1016/j.ces.2007.09.020.
29. Petrasch, J., Meier, F., Friess, H., and Steinfeld, A., "Tomography based Determination of Permeability, Dupuit–Forchheimer Coefficient, and Interfacial Heat Transfer Coefficient in Reticulate Porous Ceramics," *Int. J. Heat Fluid Flow* 29, no. 1 (2008): 315-326, doi:10.1016/j.ijheatfluidflow.2007.09.001.
30. Kočí, P., Isoz, M., Plachá, M., Arvajová, A. et al., "3D Reconstruction and Pore-Scale Modeling of Coated Catalytic Filters for Automotive Exhaust Gas Aftertreatment," *Catalysis Today* 320 (2019): 165-174, doi:10.1016/j.cattod.2017.12.025.
31. Heywood, J.B., *Internal Combustion Engine Fundamentals* (McGraw-Hill, 1988), ISBN:0-07-028637-X.
32. Sutherland, W., "LII. The viscosity of Gases and Molecular Force," *The London, Edinburgh, and Dublin Philosophical Magazine and Journal of Science* 36, no. 223 (1893): 507-531, doi:10.1080/14786449308620508.
33. Jones, O.C. Jr., "An Improvement in the Calculation of Turbulent Friction in Rectangular Ducts," *J. Fluids Eng.* 98, no. 2 (1976): 173-180, doi:10.1115/1.3448250.
34. Massey, B., Ward-Smith, J., *Mechanics of Fluids 7th Edition*, (Stanley Thornes, 1998) 275-276, ISBN: 0-7487-4043-0.
35. Kozeny, J., "Ueber kapillare Leitung des Wassers im Boden," *Sitzungsber Akad. Wiss., Wien* 136, no. 2a (1927): 271-306.
36. Carman, P.C., "Fluid Flow through Granular Beds," *Transactions, Inst. Chem. Eng.* 15 (1937): 150-166, doi:10.1016/S0263-8762(97)80003-2.
37. Carman, P.C., *Flow of Gases through Porous Media* (Butterworths, 1956). https://books.google.co.uk/books?id=F47CtAEACAAJ.

38. Ergun, S. and Orning, A.A., "Fluid Flow through Randomly Packed Columns and Fluidized Beds," *Ind. Eng. Chem.* 41, no. 6 (1949): 1179-1184, doi:10.1021/ie50474a011.
39. Ozgumus, T., Mobedi, M., and Ozkol, U., "Determination of Kozeny Constant Based on Porosity and Pore to Throat Size Ratio in Porous Medium with Rectangular Rods," *Eng. App. Comp. Fluid Mech.* 8, no. 2 (2014): 308-318, doi:10.1080/19942060.2014.11015516.
40. Rumpf, H.C.H. and Gupte, A.R., "Einflüsse der Porosität und Korngrößenverteilung im Widerstandsgesetz der Porenströmung," *Chem. Ing. Tech.* 43, no. 6 (1971): 367-375, doi:10.1002/cite.330430610.
41. Davies, C.N., "The Separation of Airborne Dust and Particles," *IMechE Proceedings* 167, no. 1b (1953): 185-213, doi:10.1177/002034835316701b13.
42. Kuwabara, S., "The Forces Experienced by Randomly Distributed Parallel Circular Cylinders or Spheres in a Viscous Flow at Small Reynolds Numbers," *J. Phys. Soc. Japan* 14 (1959): 527-532, doi:10.1143/JPSJ.14.527.
43. Knudsen, M., "Die Gesetze der Molekularstromung und der inneren Reibungsstromung der Gase durch Rohren," *Ann. Physik* 28 (1909): 75-130, doi:10.1002/andp.19093330106.
44. Moghaddam, R.N. and Jamiolahmady, M., "Slip Flow in Porous Media," *Fuel* 173 (2016): 298-310, doi:10.1016/j.fuel.2016.01.057.
45. Lee, K.W., Reed, L.D., and Gieseke, J.A., "Pressure Drop Across Packed Beds in the Low Knudsen Number Regime," *J. Aerosol Sci.* 9, no. 6 (1978): 557-565, doi:10.1016/0021-8502(78)90021-6.

Contact Information

Samuelsc2@uni.coventry.ac.uk
Coventry University
Priory St.
Coventry
CV1 5FB

Acknowledgements

A special thanks go to all contributing authors for their guidance and invaluable advice. Additionally, thanks are due to Johnson Matthey for supplying the substrates used in the project.

Abbreviations

CFD - Computational fluid dynamics
DPF - Diesel Particulate Filter
DNS - Direct Numerical Simulation
GPF - Gasoline Particulate Filter
MFR - Mass Flow Rate
VFM - Viscous Flow Meter

Symbols

a - Cell pitch, m
A_1 - Channel cross-sectional area, m^2
A_2 - Cross-sectional before contraction and after expansion, m^2
α - Fitting coefficient
β - Fitting coefficient, Forchheimer coefficient
D - Physical length scale, m
d_c - Characteristic spherical dimension, m
d_f - Diameter of fibre, m
d_h - Hydraulic diameter, m
d_p - Particle size, m
$\bar{D}_{p2}^2$ - Diameter of spheres with average surface area, m
F - Friction correction factor = 28.454
ΔP - Pressure drop, Pa
ϵ - Porosity
k - Permeability, m^2
k_0 - No-slip permeability, m^2
k_B - Boltzmann's constant, $1.38x10^{-23}$ J/K
k_k - Kozeny constant
Kn - Knudsen number
L - Channel length, m
l_{ch} - Characteristic length scale, m
λ - Molecular free mean path length, m
MPS - Mean pore size, µm
P - Pressure, Pa
Re_c - Channel Reynolds number
Re_p - Pore Reynolds number
SCF - Stokes-Cunningham Factor
σ - Collision diameter, m
μ - Dynamic viscosity, Pa.s
ν - Dynamic viscosity, m^2s^{-1}
T - Temperature, K
w - Wall thickness, m
U - Channel velocity, m/s
U_w - Wall velocity, m/s
ζ - Contraction/Expansion coefficient

© 2023 SAE International and SAE Naples Section. All rights reserved. No part of this publication may be reproduced, stored in a retrieval system, or transmitted, in any form or by any means, electronic, mechanical, photocopying, recording, or otherwise, without the prior written permission of SAE International.

Positions and opinions advanced in this work are those of the author(s) and not necessarily those of SAE International. Responsibility for the content of the work lies solely with the author(s).

ISSN 0148-7191